SIMULTANEOUS LOCAL NANO-HEATING/THERMOMETRY BASED ON PLASMONIC MAGNETOCHROMIC NANODOMES

Zhi Li,[1,4] Alberto Lopez-Ortega,[2] Antonio Aranda-Ramos,[3] José Luis Tajada,[1] Jordi Sort,[4,5] Carme Nogues,[3] Paolo Vavasori,[2,6] Josep Nogues,[1,5] and Borja Sepulveda[1]**

[1]Catalan Institute of Nanoscience and Nanotechnology (ICN2), CSIC and BIST, Campus UAB, Bellaterra, 08193 Barcelona, Spain*
[2]CIC nanoGUNE, E-20018 Donostia-San Sebastian, Spain
[3]Departament de Biologia Cel·lular, Fisiologia i Immunologia, Facultat de Biociències, Universitat Autónoma de Barcelona, Bellaterra, 08193 Barcelona, Spain.
[4]Departament de Física, Facultat de Ciències, Universitat Autònoma de Barcelona, Bellaterra, 08193 Barcelona, Spain.
[5]ICREA, Pg. Lluís Companys 23, 08010 Barcelona, Spain.
[6]IKERBASQUE, Basque Foundation for Science, E-40013 Bilbao, Spain

Keywords: Nanothermometry, Nanoheating, Nanoplasmonics, Nanomagnetism, Magnetoplasmonics, Photothermal actuation

A current strategic goal to improve the efficacy of nanotherapies is achieving externally controlled and localized therapeutic actions and, simultaneously, monitoring their induced therapeutic effects in real time and with high precision. Relevant examples are optical hyperthermia for cancer treatments and temperature-activated drug delivery. These therapies typically exploit the plasmon-enhanced light absorption in plasmonic nanoparticles at their resonant wavelength to locally produce heat for generating the therapeutic effect. Photo-thermal therapies require accurate control over the optically induced temperature changes to avoid healthy tissue damage and to minimize unwanted necrotic cell deaths. Thereby, the efficient light-heat conversion requires simultaneous accurate measurement of the local temperature at the irradiated site. While efficient optical heating can be easily achieved with a variety of noble-metal nanoparticles, precise and simultaneous non-contact local thermometry remains an issue due to the low accessibility of the irradiated regions. Current approaches to achieve non-contact and minimally invasive nanothermometry are mainly based on the detection of ratiometric or

emission lifetime variations in luminescent probes.[1–10] Nevertheless, luminescent nanothermometers can exhibit problems of stability due to photobleaching in organic dyes or blinking in quantum dots, in addition to their potential long-term cytotoxicity. Moreover, temperature detection *in-vivo* can be hampered by the large absorption and scattering by physiological tissues of the ultraviolet and visible light typically involved in the luminescent nanothermometry. To maximize light penetration, luminescent probes with absorption and emission bands in the near infrared (NIR)[11,12] have been proposed.[13–15] However, an additional drawback of ratiometric and lifetime luminesce nanothermometers is the cost and complexity of the detection systems. In addition, none of these aforementioned approaches targets the strategic nanotherapeutic goal of enabling local heating and simultaneous real-time temperature detection. Although this approach remains technologically challenging, as an example in this direction, luminescent nanothermometers have been attached to plasmonic nanostructures to enable local heating and detection of the induced temperature variations.[11,16] Nevertheless, the temperature detection suffers the same limitations of luminescent thermometry, in addition to the potential quenching or absorption of the emitted light by the plasmonic nanostructures, or the necessity of using different light sources for thermometry and heating. Nanoparticles based on Ln^{3+} cations have also shown heating and thermometry capacity using NIR fluorescence absorption and emission bands, although the simultaneous heating and detection can only be achieved at different wavelengths.[11] Besides, their optical heating efficiency is substantially lower than that of plasmonic nanoparticles.

Here we present a novel and cost effective magnetochromic nano-heating/thermometry concept based on magnetoplasmonic nanodomes, which are composed of 100 nm diameter polystyrene beads partially coated with a ferromagnetic/Au multilayer. In particular, we have studied

nanodomes coated with a [Co-1nm/Au-6 nm]x5/Au-5nm or [Fe-5 nm/Au-35nm] multilayers (**Figure 1**a-c). Their nanofabrication, based on a combination of electrostatic self-assembly of the polystyrene beads and highly directional electron beam evaporation (Figure S1), enables creating nanoparticles that merge strong optical and magnetic anisotropies with a nearly spherical shape (see Methods in Supporting Information). These magnetoplasmonic nanodomes embody very high thermo-plasmonic heating efficiency and allow very accurate, stable and fast detection of the local temperature variations. The nanothermometry is achieved by measuring the viscosity-dependent rotation dynamics of nanodomes activated by a weak external AC magnetic field. The magnetic rotation of the nanodomes results in an intense modulation of the transmitted light owing to their strong magnetochromic effect, *i.e.* the large spectral change of the colloidal dispersion when a magnetic induction B is applied. Indeed, we show that ultraprecise nanothermometry is achieved while optically heating the nanodomes through an innovative analysis of the temperature-induced viscosity changes of the liquid surrounding the nanodomes. Such intense magnetochromic effect, together with the fast rotation speed of the nanodomes and their high heating efficiency, enable the simple and highly sensitive simultaneous plasmonic heating and temperature detection, even for low particle concentrations and in highly inhomogeneous media (*e.g.* tissues or physiological fluids).

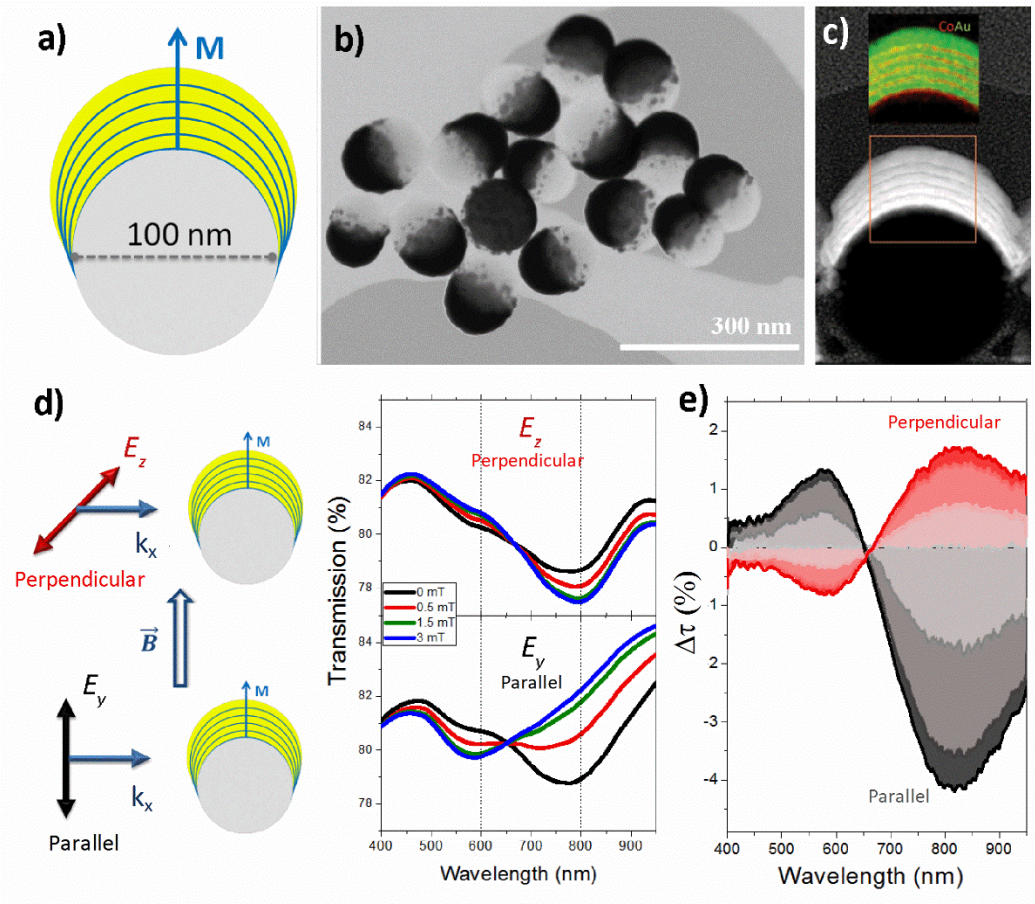

Figure 1. a) Schematic of the Co/Au nanodomes with out-of-plane magnetization. b) and c) High-resolution TEM images and energy-dispersive X-ray elemental mapping (inset in panel c) of the nanodomes with the [Co/Au] multilayers. d) Transmission, τ, spectra of nanodomes in water under a static B when the light polarization E is either perpendicular or parallel to B, and the light wave vector k is perpendicular to B, as shown schematically. e) Spectra of the transmission variations ($\Delta\tau=\tau(B)-\tau(0)$) induced by the static B for the perpendicular (red curves) and the parallel (black curves) polarizations.

High-resolution transmission electron microscopy (TEM) and energy-dispersive X-ray (EDX) elemental mapping images of Figure 1b and 1c clearly show the half magnetoplasmonic shell made of alternating layers with different composition and the nearly spherical shape of the nanodomes. The magnetoplasmonic multilayer provides the highly anisotropic magnetic and optical properties. The set of intercalated Co nanolayers exhibits an out-of-plane magnetic anisotropy, as indicated by the hysteresis loops of Figure S2.[17] In addition, the optical anisotropy is given by the existence of two localized plasmonic resonances with different resonant wavelengths along two different and orthogonal axes of the nanodomes (Figure 1d and Figure S3). According to the Finite Difference Time Domain (FDTD) analysis, these resonances are located at 600 nm and 800 nm (Fig. S3), and are excited when the polarization *E* of the incident light is either parallel or perpendicular to the plane of the [Co/Au] multilayer. These resonances are in excellent agreement with the measured transmission spectra dips in Fig. 1d.

This combination of features is crucial for attaining intense magnetochromic effects (Figure 1d), which can be rapidly modulated (at hundreds of Hz). As a result of the magnetic anisotropy, the nanodomes that are initially randomly oriented in solution can be aligned with their *M* parallel to the applied magnetic induction, *B,* via magnetic torque. Such alignment enables a very accurate control of the excited plasmonic resonance with a linearly polarized light beam. The magnetochromic effect can be clearly observed in Figure 1d, which shows the strong changes in the transmission spectrum through a diluted colloidal dispersion (concentration of $1 \cdot 10^9$ nanodomes/mL) as a function of the amplitude of B for the light propagation wave vector (*k*) perpendicular to *B*, and the polarization *E* either parallel or perpendicular to *B*. In the parallel configuration, *i.e.* light polarization *E* parallel to *B*, a dip in the transmission at 600 nm is observed, whereas the dip is located at 800 nm in the perpendicular configuration, *i.e.* light

polarization E perpendicular to B, as predicted by the FDTD simulations. Interestingly, a B amplitude as low as 2 mT allows toggling between the parallel and perpendicular resonances located at 600 nm and 800 nm. As a result, the transmission spectrum can be continuously tuned between the two resonances by modifying B amplitude (Figure 1d), with the largest spectral variation at ~810 nm (Figure 1e). The intense 4% transmission variation ($\Delta\tau = \tau(B) - \tau(0)$) at 810 nm can be drastically amplified by increasing particle concentration. Although sizable magnetochromic effects can be obtained by applying the magnetic field in different directions (Figure S4), we focus on the configuration with B parallel to E (**Figure 2**a), which is the one producing the largest magnetochromic effect at 810 nm. In addition, this optimal wavelength is within the tissues transparent window, and is spectrally close to commercially available and low-cost laser diodes with emission at 808 nm.

The application of a low amplitude (2 mT) alternating B with frequency ω induces the rotation of the nanodomes (Figure 2a), which results in an intense modulation of the transmitted intensity of the 808 nm linearly polarized laser beam. Importantly, the necessary B can be easily generated by a small coil, and the nanodomes rotation detection only requires a single linearly polarized light beam with 808 nm wavelength to maximize the magnetochromic effect, and a conventional photodiode (see Supporting Information).

The right panel in Figure 2a depicts the dependence of the magnetochromic effect for incident light with 808 nm wavelength under an alternating B. If the B frequency is low (<100 Hz) the majority of the particles are oriented parallel to B when the magnetic induction is at its maximum amplitude $\pm B_{max}$ (Figure 2a). In these conditions light can only excite the plasmonic resonance located at 600 nm wavelength and, therefore, the transmitted intensity is maximized for the

incident light with 808 nm wavelength (see Figure 1d). When the magnetic induction transitions between $+B_{max}$ and $-B_{max}$, the particles flip their orientation (Figure 2a). During the transition the resonance located at 800 nm is excited, thereby efficiently absorbing and scattering the incident light with 808 nm wavelength. As a result, a large decrease of the transmitted intensity is observed (Figure 2a). As the extinction cross-section of the Co/Au nanodomes for $\pm B_{max}$ orientations is completely equivalent, an alternating B with ω frequency generates a light transmission modulation at frequency 2ω (see Figure 2a).

The periodic transmittance variation enables using the Fast Fourier Transform (FFT) analysis to extract both the amplitude and phase lag with respect to B for the different harmonics of the transmittance (Figure S5). Since the nanodomes are dispersed in a viscous medium, the magnetochromic modulation amplitude and phase lag strongly depend on the frequency of B. Figure 2b represents the frequency dependence of the amplitude ($A2\omega$) and phase lag ($\phi 2\omega$) of the second harmonic (2ω). In this analysis, the amplitude $A2\omega$ is normalized by the DC component of the FFT to eliminate the influence of the intensity fluctuations in the incident light, and it is therefore dimensionless. $A2\omega$ has the typical bell-like shape of resonant phenomena, which is due to the Brownian relaxation in this case[18,19]. The maximum of $A2\omega$ is observed at 700 Hz, and for higher frequencies $A2\omega$ presents a monotonic decrease, which manifests the difficulty of nanodomes to follow B due to the viscous damping. The influence of the viscosity is also evident in the phase lag plot, $\phi 2\omega$ (Figure 2b), showing a monotonic increase of the phase difference as ω increases, being almost 2π at 2 kHz.

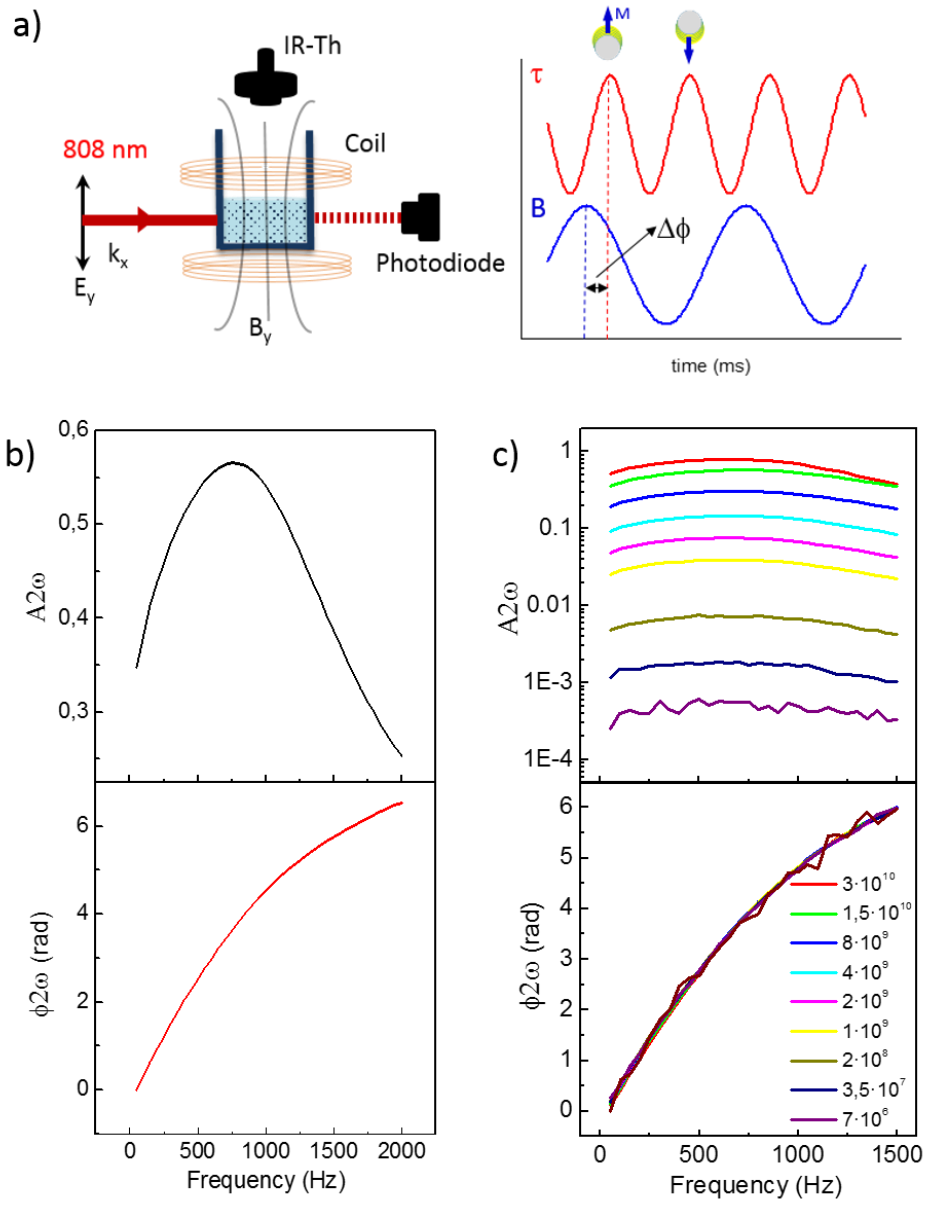

Figure 2. a) left -Schematics of the experimental set-up; right – Rotation of the Co/Au nanodomes under an alternating B and the induced light transmission (τ) modulation. b) Variation in the amplitude $A2\omega$ and phase lag $\phi 2\omega$ of the transmitted intensity second harmonic (2ω) with ω. c) Nanodomes concentration dependence of $A2\omega$ and $\phi 2\omega$ as a function of ω.

Interestingly, moderate particle concentrations ($3 \cdot 10^{10}$ particles mL^{-1}) show huge transmittance modulation amplitudes, close to 90% (*i.e.* $A2\omega \approx 0.9$), which is orders of magnitude larger than those achieved in magneto-optic effects in magnetoplasmonic nanoparticles,[20–23] and requires a much lower B amplitude. A key consequence of the strong magnetochromic modulation is the effectiveness to detect extremely low nanodome concentrations (Figure 2c), even below 10^7 particles$\cdot mL^{-1}$ (*i.e.*, well below the detection limit of high-end UV-vis spectrometers; Figure S6), by using a very simple and cost-effective set up. Nevertheless, probably the most interesting and relevant feature for sensing applications is the complete independence of $\phi 2\omega$ on the nanodome concentration (Figure 2c).

Since $\phi 2\omega$ depends only on the viscous damping, the quantification of the $\phi 2\omega$ changes is an appealing approach to detect local viscosity variations around the nanoparticles. As expected, $\phi 2\omega$ approaches towards 2π at lower frequencies as the viscosity η (and thus, the damping) increases (**Figure 3a**). This effect is accompanied by a shift in the $A2\omega$ maximum to lower frequencies (Figure S7a). For small viscosity changes ($\Delta\eta < 1$ mPa·s) the phase lag variation at a given frequency, $\Delta\phi 2\omega$, is approximately linear. Interestingly, the induced $\Delta\phi 2\omega$ in this small η range is maximized at a ω = 600 Hz, when B = 2 mT (Figure S7b). Therefore, the sensitivity to detect the local viscosity variations, which is defined as $S_\eta = \Delta\phi 2\omega / \Delta\eta$, is maximized at 600 Hz, giving a value of 0.95 rad$\cdot$(mPa·s)$^{-1}$ for $\Delta\eta$ < 1 mPa·s. For larger viscosity changes, $\phi 2\omega$ displays a non-linear relationship with respect to the liquid viscosity (Figure 3b).

The detection of $\Delta\phi 2\omega$ at a fixed frequency has the additional advantage of enabling real-time monitoring of local viscosity changes (Figure 3c). Considering the signal-to-noise ratio of $\phi 2\omega$, we can determine that the detection limit of the viscosity variations, defined as $LOD_\eta = 3\sigma / S_\eta$

(where is σ is the noise; Figure S8), is as low as 0.0016 mPa·s. This detection limit is 60-fold smaller than that of state-of-the-art plasmonic nanorheometers.[24] Besides the strong magnetochromic effect, this exceptional LOD value is also due to the high rotation frequency of our nanodomes at the sensitivity maximum, which reduces the detrimental effects of low frequency noise, especially the 1/f noise. This is a clear advantage with respect to micron-sized particles[25] or long magnetic nanowires, which cannot rotate at such a high frequency,[26,27] and highlights the importance of the spherical geometry and small size of the nanodomes. Importantly, the introduction of electronic filters or lock-in amplifiers could reduce even further this detection limit. As can be observed in Fig. 3b, there is a large decrease in the sensitivity to detect the viscosity variations for large liquid viscosities (η > 5 mPa·s). As a result, we can establish that the working viscosity range of the magnetochromic nanodomes as nanorheometers is from 0.1 mPa·s to 5 mPa·s, which is adequate for the biomedical applications.

The high sensitivity to detect viscosity variations opens the path to monitor the local temperature (T) changes by exploiting the reduction of water viscosity when T increases. We thereby measured $\phi 2\omega$ at different water T by heating the nanodomes dispersion with a Peltier-heater (Figure 3d-f) and we monitored the ΔT with a calibrated IR-thermometer (Figure 2a). In this case the variation of $\phi 2\omega$ with T shows a maximum at $\omega \approx$ 700 Hz for B = 2 mT (Figure S9). The small frequency shift of the maximum sensitivity with respect to the viscosity measurements is due to the small non-linearity of $\phi 2\omega$ with respect to the viscosity, and the smaller and negative values of the $\Delta\eta$ induced by a T increase. Thus, the maximum sensitivity in the detection of temperature changes, ΔT, defined as $S_T = \Delta\phi 2\omega/\Delta T$, corresponds to -0.028 rad/°C for small T variations (<10°C) around room temperature.

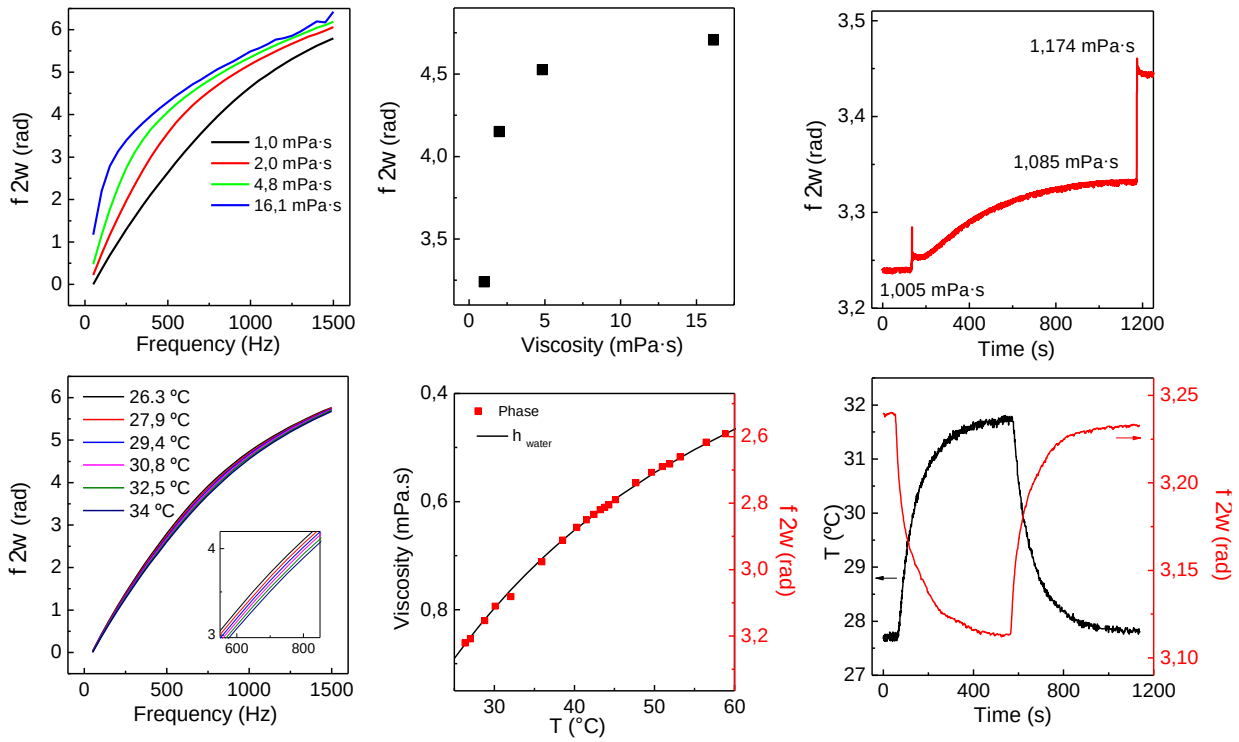

Figure 3. a) Frequency dependence of $\phi 2\omega$ for water/glycerol solutions of different viscosities. b) $\phi 2\omega$ for the same water/glycerol solutions at fixed 600 Hz actuation frequency (B = 2 mT). c) Real-time detection of small viscosity variations. d) Frequency dependence of $\phi 2\omega$ for different water temperatures (Inset: zoom of $\phi 2\omega$ for 600-800 Hz). e) Temperature calibration curve of the nanothermometers, showing the variations of $\phi 2\omega$ measured at 700 Hz as a function of the water T, compared to the tabulated water viscosities as a function of T. f) Real-time detection of the temperature variation induced by an external Peltier heater by monitoring $\phi 2\omega$ at 700 Hz modulation. (Particle concentration $6 \cdot 10^9$ nanodomes/mL).

The calibration curve of Fig. 3e enables direct conversion between $\phi 2\omega$ and the fluid temperature to obtain quantitative determination of the temperature changes. Even though the water viscosity is not a linear function of T (Fig. 3e), $\phi 2\omega$ shows an almost linear dependence in the interesting T range for biomedical applications (*i.e.,* from 37ºC to 45ºC). To quantify larger T changes (>20ºC), the variation of the sensitivity with T should be considered, as pointed out in the calibration curve of Fig. 3e. For large water temperatures (T > 60ºC), the decrease in the sensitivity to detect small T changes (*i.e.*, 2.8-fold from 25ºC to 60ºC) can be compensated by the capacity to induce the particle rotation at higher frequencies by exploiting the substantially lower fluid viscosity. The faster opto-magnetic modulation enables reducing the noise in $\phi 2\omega$, thereby compensating the lower sensitivity and minimizing the increase in the detection limit.

Similarly, we can use $\phi 2\omega$ at a fixed frequency, 700 Hz, to monitor in real-time the temperature variations. Figure 3f compares the $\phi 2\omega$ variation generated by the ΔT with the measurements of the calibrated IR-thermometer, showing that both temperature curves exhibit a similar temporal evolution. Considering the sensitivity and noise of $\phi 2\omega$ at 700 Hz (Figure S8), we can establish a limit of detection of temperature variations LOD_T = 0.05 ºC, which is in the same range as that of state-of-the-art luminescent nanothermometers[2,16,28] although using a much simpler and lower cost detection system.

The working temperature range of this nanothermometry concept corresponds to the temperature interval in which H_2O is in the liquid state (*i.e.,* from 0 ºC to 100 ºC, at atmospheric pressure). This range can be expanded by adding liquids that either reduce the water freezing T (*e.g.* ethanol) or increase the boiling T (*e.g.* glycerol), as long as the fluid viscosity is below 5 mPa·s to enable the efficient magnetic rotation of the nanodomes.

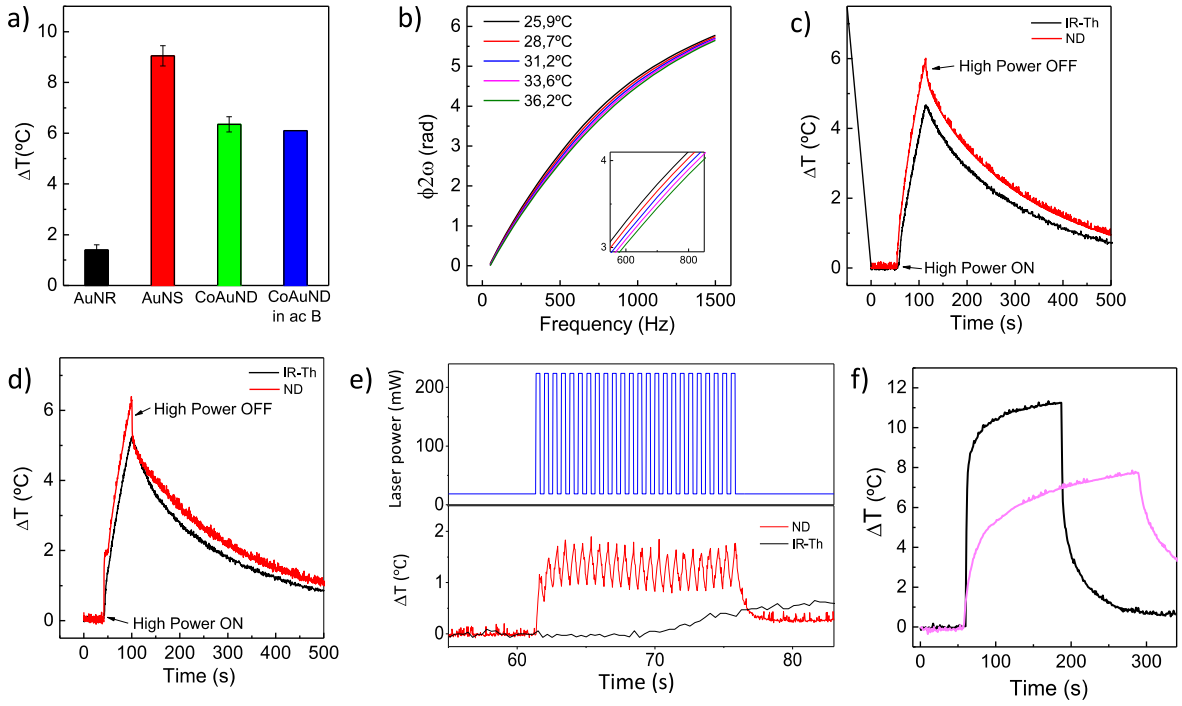

Figure 4. a) Comparison of the optical heating efficiency of Co/Au nanodomes (CoAuND), Au nanorods (AuNR), and Au nanoshells (AuNS), having resonances at *ca.* 800 nm wavelength under a linearly polarized laser (808nm, 315 mW). b) $\phi 2\omega$ as a function of ω for different liquid T induced by plasmonic heating using increasing laser power (25, 75, 125, 175, 225 mW). c) Comparison of the real-time detection of the ΔT by $\phi 2\omega$ at 700 Hz and the IR-Th induced by a sudden increase in laser power (from 25 mW to 315 mW) of a collimated laser beam and d) of a focused laser beam. e) Detection of fast ΔT by the focused laser with pulsed laser power of 600 ms period. The ΔT detected by the nanodomes is extracted from $\Delta T = \Delta\phi 2\omega / S_T$. (Particle concentration $6 \cdot 10^9$ nanodomes/mL). f) Comparison of the simultaneous local optical heating and temperature detection inside a microfluidic channel by a focused light beam (black curve) and a large light beam (magenta curve) under a laser power increase from 15 mW to 185 mW.

Another relevant advantage of the nanodomes is their capacity to detect ΔT by using the very same NIR light beam employed for heating *via* thermo-plasmonic effects. Indeed, Figure 4a shows that the nanodomes are also excellent thermo-plasmonic heaters in the NIR, showing heating efficiencies in the same range as those of state-of-the-art optical nanoheaters,[29,30] such as Au nanorods and nanoshells.[31–33] Remarkably, the magnetic modulated rotation of the nanodomes only induces a weak 4% reduction of the heating efficiency compared to the randomly oriented nanodomes. Therefore, the combined strong optical absorption efficiency and high sensitivity to detect local viscosity variations can be exploited to achieve the nanotherapeutic strategic goal of simultaneously inducing local optical heating and detecting the ΔT caused by the same NIR light beam at the illuminated region. Figure 4b demonstrates this ability by displaying the frequency dependence of $\phi 2\omega$ at different laser powers, once the equilibrium T in the colloidal dispersion measured by the IR-thermometer is reached after 20 min. As in the Peltier heating case, the maximum sensitivity to detect ΔT occurs at 700 Hz, and it has a value of -0.028 rad/°C (Figure S9). Moreover, Figure 4c displays the real-time detection of the ΔT extracted from $\phi 2\omega$ at 700 Hz for a sudden power increase (from 25 mW to 315 mW) of the collimated 808 nm laser beam (spot diameter 2 mm), compared to the IR-thermometer measurements. A steeper ΔT is observed during the first 2 seconds in the $\phi 2\omega$ measurements when the laser power abruptly increases (Figure S10a), clearly showing that the nanodomes detect earlier the ΔT due to their local sensitivity, while the IR-thermometer only detects the averaged ΔT at the liquid surface.

Remarkably, this latter feature enables accessing fast (millisecond) and local dynamic ΔT caused by the laser that cannot be observed by conventional IR non-contact thermometers. The faster

and local response of $\phi 2\omega$ to ΔT can be further appreciated by noting the substantially more pronounced differences in the detection of dynamic ΔT between the nanodomes and the IR-thermometer when the laser is focused in a small spot (*ca.* 0.5 mm in diameter) (Figures 4d and 4e). Whereas the IR-thermometer shows a similar ΔT curve as that in Figure 4c under an identical abrupt laser power change, the local temperature around nanodomes suffers an even steeper increase than in Figure 4c, within the first 500 ms (Figure S10b), which is followed by a sudden reduction in the slope during the following 7 s. We attribute the very sharp initial increase to the detection of the fast temperature increase in the liquid surrounding the particles at the focal spot, which have the highest light intensity. Such strong localized heating triggers a convective flow process,[34–36] which ejects the hot particles and liquid from the focus. The ejected hot particles are then substituted by colder particles and liquid, thereby explaining the sudden reduction of the slope when the convection process starts. Once the convection is stabilized, a process that takes *ca.* 7 s, the temperature acquired by the nanodomes and the IR-thermometer start exhibiting similar slopes. Likewise, when the laser power suddenly decreases, a steep temperature decrease is observed within the first second due to the local cooling triggered by the convection process, which cools down the focal point inside the liquid before the surface of the liquid dispersion that is monitored by the IR-thermometer.

The capacity to detect fast local ΔT at the focal point is also corroborated in Figure 4e, which shows the temperature detection by nanodomes under a pulsed laser excitation with square shape and 600 ms period. The fast acquisition (31 measurements second in this experiment), enables us to clearly observe the millisecond-scale temperature oscillations in the focus under the modulated laser power, which cannot be detected in the IR-thermometer.

To highlight the local character of the nanodomes nano-heating/thermometry concept we analyze in Figure 4f the optical heating and temperature detection inside a microfluidic channel with 0.8 mm height, which is not accessible to the non-contact IR-thermometer. We have compared the temperature changes induced by a 1 mm diameter light beam and a focused light beam by a microscope objective with a numerical aperture of 0.6 in air, which yields a spot size of several μm^2 inside the microfluidic channel. As can be observed, the focused light beam generates a much faster local temperature increase due to the higher intensity of the light beam in the focus. The faster cooling process induced by the large temperature gradient also evidences the localized heating and temperature detection that can be achieved with the nanodomes.

To demonstrate the potential of the magnetochromic nano-heater/thermometers in biomedical applications, we show their capability to simultaneously heat and detect the temperature variations in concentrated monocyte cell dispersions. Notably, such cell dispersions show very strong light scattering to mimic the challenging optical conditions of physiological tissues. Indeed, the monocyte cell dispersions are an even more challenging optical media than tissues composed of adherent cells due to the dynamic and random perturbations in light scattering caused by free cell movement and cell sedimentation with time.

We first analyze the features and the stability of the magnetochromic modulation in the cell medium. The frequency dependence of $A2\omega$ shows the maximum at 300 Hz (**Figure 5**a), which reflects both the higher viscosity of the cell medium compared to that of water, and the increase of the mass and hydrodynamic radius of the particles due to the unspecific adsorption of proteins at the nanodomes surface. Remarkably, the nanodomes show very high stability in cell medium,

as it is demonstrated by the high stability of $A2\omega$ and $\phi 2\omega$ measurements at 300 Hz for more than 2 hours (Figure S11).

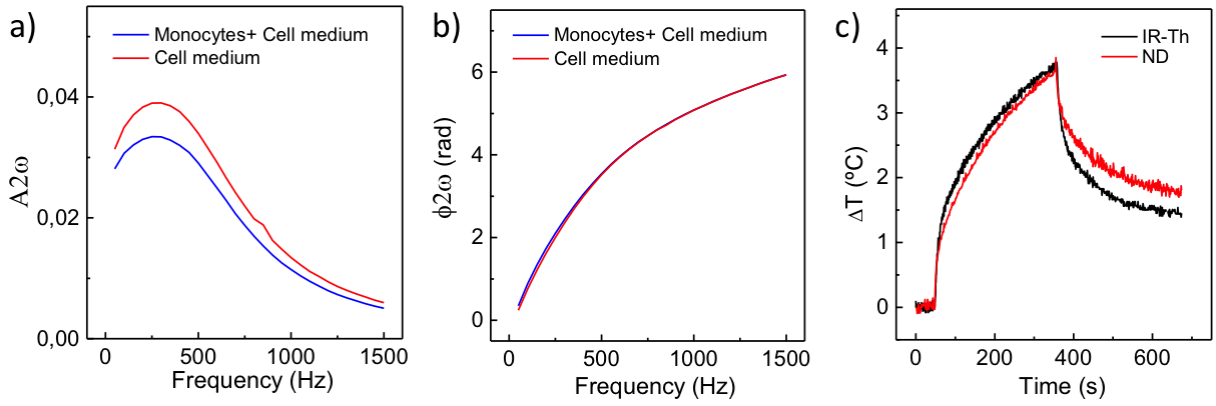

Figure. 5 a) and b) Frequency dependence of $A2\omega$ and $\phi 2\omega$, respectively, for $1.7 \cdot 10^9$ nanodomes·mL^{-1} in a cell medium and in a monocyte cell dispersion with $6 \cdot 10^6$ cells·mL^{-1}. e) Comparison of the real-time detection of ΔT induced by a 225mW increase of the 808nm laser power by the nanodomes $\phi 2\omega$ ($\Delta T = \Delta\phi 2\omega / S_T$) and the IR-thermometer in the monocytes dispersion.

Next, we introduce a concentration of $1.7 \cdot 10^9$ nanodomes/mL (equivalent to 10 µg/mL of nanodomes) in a monocyte cell dispersion with high cell concentration ($6 \cdot 10^6$ cells/mL). The total transmitted light intensity through the monocytes dispersion decreases 20-fold with respect to that in water due to the large light scattering generated by the cells. Despite such intensity reduction, both $A2\omega$ and $\phi 2\omega$ can be easily detected (Figs. 5a and 5b). These measurements show that the $A2\omega$ maximum is located at the same frequency as in the case of the cell medium without monocytes, i.e. 300 Hz, thereby implying similar viscosities, as expected since the

internalization of nanodomes by the cells is negligible during the assay time (20 min). Likewise, the temperature variations caused by the laser can be detected and monitored in real-time, as shown Fig. 5c. Despite the 20-fold reduction in the transmitted intensity, the noise of $\phi 2\omega$ only shows a 3-fold increase, thereby yielding a detection limit of 0.15 °C of the temperature variations in the concentrated cell dispersion, which is sufficient for controlling the therapeutic effect in photo-thermal therapies. Such small increase in the detection limit is remarkable considering the low concentration of the nanodomes and the strong light scattering of the cell dispersion. In the case of tissues composed of adherent cells and for larger particle concentrations, a smaller detection limit (closer to 0.05ºC) is expected.

Although the Co content in the nanodomes might raise toxicity concerns for biomedical applications, the cytotoxicity is expected to be minimal due to the low Co amount, and its protection by the thick Au films. Nevertheless, to minimize any potential toxicity, we have demonstrated that the simultaneous nano-heating/thermometry can also be achieved with non-toxic Fe/Au nanodomes. The optical heating efficiency of the Fe/Au nanodomes is similar to that of the [Co/Au] nanodomes and, although the magnetochromic amplitude $A2\omega$ is 3-fold smaller due to the in-plane magnetization in the Fe layer (Figure S12a,b), we can monitor ΔT with similar sensitivity (-0.025 rad/ºC) and a detection limit of 0.08 ºC in water (Figure S12c), thereby highlighting the biomedical potential of this nanotechnology.

Although the magnetochromic nanodomes cannot simultaneously determine the absolute values of the temperature and the fluid viscosity, this is not a limitation to control the temperature increase during photo-thermal therapies. The strategy for T control *in vivo* will be to determine first the frequency dependence of both $A2\omega$ and $\phi 2\omega$ at low optical power (i.e., negligible

heating). These measurements will determine the magnetic frequency that maximizes both the opto-magnetic signal and the sensitivity to detect the ΔT. Taking such $\phi 2\omega$ value as reference, then the optical power will be increased to generate the local temperature increase. The usual duration of the optical treatments is between 10 min to 30 min, which is short compared to the physiological responses (typically in the hours range). As a consequence, it can be assumed that any change in the viscosity during the optical treatment will be only the result of the temperature increase and not due to any physiological effect. Hence, the observed $\phi 2\omega$ reduction will be only due to the local temperature increase. Moreover, high local viscosity variations are not expected due to the nanoscale size of the probes.[24] As the nanodomes are much smaller than the cells, they are only sensitive to the viscosity variations of the interstitial fluid, which is mainly composed of water, salts, proteins, and carbohydrates. This effect is clearly observed in Fig. 5a, which shows that the frequency dependence of $A2\omega$ and $\phi 2\omega$ are exactly similar in the case of the cell medium and in the monocyte cell dispersion with high cell concentration ($6 \cdot 10^6$ mL^{-1})

Summarizing, we have demonstrated a new integrated magnetochromic nano-heating/thermometry concept, which simultaneously shows very high heating efficiency and sensitivity in the detection of temperature variations. The integrated concept is based on the innovative detection of tiny viscosity variations around magnetoplasmonic (Co/Au and Fe/Au) nanodomes when they are optically heated, by exploiting the intense magnetochromic modulation conferred by their concurrent high magnetic and optical anisotropies. The cost-effectiveness and the fabrication scalability, together with the simplicity and low cost of the detection system add more relevance to this powerful tool to detect low temperature variations in highly inhomogeneous media with low accessibility. Remarkably, the magnetochromic nano-heater/thermometers have been able to merge detection limits in temperature variations similar to

the best luminescent nanothermometers, but with a much simpler and cost-effective set-up, and optical heating efficiencies comparable to that of state-of-the-art plasmonic nanoheaters.

The spherical shape and small size of the nanodomes confers them a low invasiveness and the capacity to rotate at high frequencies, which represents important advantages with respect to other possible nano-heater/thermometer approaches. As a result, the magnetoplasmonic nanodomes have a high potential for controlling and real-time monitoring photo-thermal therapies and optically triggered drug delivery systems. The nanodomes could also be interesting for miniaturized bioassays in biosensing applications.[19]

Experimental Section

Fabrication of the nano-heater/thermometers:

A schematic drawing of the different fabrication steps of the Co/Au and Fe/Au nanodomes can be seen in Figure S1. Briefly, two-inch silicon wafers (Siegert Wafer GmbH) previously cleaned with oxygen plasma (PS210, PVA Tepla America, Inc.) were used as substrates for the electrostatic self-assembly of polystyrene nanospheres. The self-assembly started by incubating the wafer surface with a solution containing positively charged polyelectrolyte [poly(diallyldimethylammonium chloride, PDDA, Sigma-Aldrich] at 2% concentration for 1 min. Then the wafer was rinsed with osmotized water and blow dried with N_2 gas, thereby yielding a monolayer of PDDA on the surface. Next, the modified wafer surface was incubated with the dispersion of sulfate functionalized polystyrene beads (100 nm diameter, concentration

0.2%, Life Technologies) for 2 min, followed by rinsing with water and drying with N_2 flow to obtain a self-assembled monolayer of nanospheres. The self-assembly process yielded homogeneous particle monolayers with short-range order and surface density of $1.6 \cdot 10^9$ spheres$\cdot$cm^{-2}, i.e., about $3.1 \cdot 10^{10}$ particles per wafer.

The nanospheres on the wafer were then coated with Co or Fe and Au layers using an electron beam evaporator (ATC-8E Orion, AJA International Inc) to form the multilayers ([Co 1 nm/Au 6 nm]x5 /Au 5 nm) or (Fe 5nm/Au 35 nm) semi-shells with a total thickness of 40 nm. The thickness of the deposited layers was monitored with Å precision by a quartz crystal microbalance during the evaporations. Finally, the coated nanoparticles were incubated, while still on the surface of the wafer, with a negatively charged polyelectrolyte [Poly (sodium 4-styrenesulfonate, PSS, Sigma-Aldrich] at 2% concentration for 3 min to deposit a monolayer of PSS on the Au surface, thereby increasing the surface charge and their hydrophilicity. The wafer was rinsed with water to remove the excess of PSS and was dried with N_2 flow. The Co/Au nanodomes were then magnetized out-of-plane by placing the wafer on a strong 7-cm diameter disk-shape NdFeB magnet. To disperse the particles in water, the wafer together with 10 mL of water is put into an ultrasonic bath for 1 min. The nanodomes were finally concentrated and re-dispersed through centrifugation (4000 rpm, 5 min), followed by ultrasonication to achieve highly stable dispersions at the required concentrations. The Si wafers could be reused after cleaning for 10 min in aqua regia, which efficiently dissolved the Co, Fe and Au layers.

Morphological, optical, magnetic and colloidal characterization:

To study the size and distribution of nanodomes on the Si wafers, scanning electron microscopy (SEM) studies were performed using Quanta SEM 650 (FEI) at 20 kV.

The TEM sample preparation was carried out on a Helios 450S SEM/FIB DualBeam (FEI, Netherlands) instrument. For x-section lamellae preparation the layer of spheres on the Si wafer were covered by ~200 nm of electron beam deposited Pt followed by ~2 μm ion beam deposited Pt. The thickness of the cross-section was intended to be no more than 20-30% of the diameter of the latex spheres in order to observe the layered structure on the curved surfaces.

The scanning transmission electron microscopy (STEM) study was performed on a Titan 60-300 TEM/STEM (FEI, Netherlands) instrument equipped with an energy dispersive x-ray (EDX) detector. The STEM imaging and the EDX mapping was carried out in STEM mode at 300 kVwith a scan step (pixel size) of 1 nm and pixel dwell time 20 ms for imaging and 200 ms for mapping.

The ultraviolet-visible (UV-vis) spectroscopy studies of the MP nanodomes dispersions were carried out using Lambda25 (PerkinElmer). For the optical measurements, the optical spectra ranged from 400 nm to 1100 nm, which covered visible light and near infrared region.

The magnetic characterization of the nanodomes was performed on monolayers of nanodomes that were transferred to adhesive tapes to eliminate the magnetic signal from the multilayer that is deposited on the wafer surface. Hysteresis loops were acquired at room temperature using a vibrating sample magnetometer (MicroSense) with a maximum applied field of $\mu_0 H = 2$ T. The measurements were performed by applying the field perpendicular or parallel to the plane of the sample, i.e., in an out-of-plane configuration.

Combined optical heating and magnetochromic analysis setup:

A custom-made opto-magnetic analysis system was used to determine the magnetochromic and photothermal effects of the nanodomes in liquid (see Figure 2a), which consisted of: i) a NIR laser diode with emission wavelength at 808 nm (L808P500MM, THORlabs) driven by a laser diode controller (LDC240C, THORlabs) and a temperature controller (TED240C, THORlabs), ii) an optical collimating and aligning system, iii) a Helmholtz coil, iv) a signal generator (SDG1025, Siglent) and a modulated power supply (TS200, ACCEL Instruments), v) a Si photodiode (PDA36A-EC, THORlabs), vi) an infrared thermometer (MLX90614), and vii) data acquisition card (National Instruments) and computer for acquisition and processing with Labview.

The NIR laser was linearly polarized after the optical collimating and aligning system, which enabled the control of laser spot size at the sample (minimum diameter: 0.5 mm). The magnetic induction applied to the sample was generated by a Helmholtz coil with diameter of 3 cm to maximize the homogeneity of the field. In the experiment either static or sinusoidal magnetic induction, with tunable frequency (0- 2 kHz), and strength (0- 2 mT) was used. The transmitted light intensity was acquired and then processed via FFT analysis in a Labview program. The parameters extracted from the FFT analysis, i.e., amplitude ($A2n\omega$) and phase ($\phi 2n\omega$), were real-time recorded. The time interval of data analysis was 250 ms, except for the high speed measurements of Figure S11, in which the time interval was 31 ms.

For the analysis, samples in different solutions (water, glycerol and cell media) with different concentration of nanodomes but with constant volume (~400 μL) were prepared. The experimental photo-thermal efficiency comparison with Au nanorods (71 nm long axis and 20 nm short axis) and Au nanoshells (120 nm diameter of SiO_2 core and 16 nm Au shell thickness) was carried out using commercial Au particles (Nanocomposix). The temperature of the solution

and the power transmitted through the sample were continuously monitored by the infrared thermometer and the photodiode. The time interval of data recording for the acquired temperature was 0.25s during the assays.

Acknowledgements

Corresponding Authors*: Borja Sepulveda (borja.sepulveda@icn2.cat) and Alberto Lopez-Ortega (a.lopezortega@nanogune.eu)

This work is supported by the Spanish MINECO projects MAT2013-48628-R, MAT2016-77391-R and PCIN-2016-093 (H2020 M-ERA.NET). Zhi Li acknowledges the Chinese Scholarship Council Program (201506950059) for financial support. The 2017-SGR-292 project of the Generalitat de Catalunya is acknowledged. The ICN2 is funded by the CERCA programme / Generalitat de Catalunya. The ICN2 is supported by the Severo Ochoa programme of the Spanish Ministry of Economy, Industry and Competitiveness (MINECO, grant no. SEV-2013-0295). A. L. O. and P. V. acknowledge funding from the Basque Government (Project No. PI2015_1_19), the Spanish Ministry of Economy and Competitiveness and the European Regional Development Fund [Project No. FIS2015-64519-R (MINECO/FEDER)]. A.L.O acknowledges the support from Juan de la Cierva grant. This work was also supported by the Spanish Ministry of Economy, Industry and Competitiveness under the Maria de Maeztu Units of Excellence Programme - MDM-2016-0618.

References

[1] X. Wang, O. S. Wolfbeis, R. J. Meier, *Chem. Soc. Rev.* **2013**, *42*, 7834.
[2] C. D. S. Brites, P. P. Lima, N. J. O. Silva, A. Millán, V. S. Amaral, F. Palacio, L. D. Carlos, *Nanoscale* **2012**, *4*, 4799.
[3] D. Ross, M. Gaitan, L. E. Locascio, *Anal. Chem.* **2001**, *73*, 4117.
[4] J. Feng, K. Tian, D. Hu, S. Wang, S. Li, Y. Zeng, Y. Li, G. Yang, *Angew. Chemie - Int. Ed.* **2011**, *50*, 8072.
[5] G. W. Walker, V. C. Sundar, C. M. Rudzinski, A. W. Wun, M. G. Bawendi, D. G. Nocera, *Appl. Phys. Lett.* **2003**, *83*, 3555.
[6] J. M. Yang, H. Yang, L. Lin, *ACS Nano* **2011**, *5*, 5067.
[7] C. H. Hsia, A. Wuttig, H. Yang, *ACS Nano* **2011**, *5*, 9511.
[8] L. H. Fischer, G. S. Harms, O. S. Wolfbeis, *Angew. Chemie - Int. Ed.* **2011**, *50*, 4546.
[9] C. L. D. Brites C D S, Millán A, in *Handb. Phys. Chem. Rare Earths*, **2016**, pp. 339–427.
[10] J. Rocha, C. D. S. Brites, L. D. Carlos, *Chem. - A Eur. J.* **2016**, *22*, 14782.
[11] L. Marciniak, A. Pilch, S. Arabasz, D. Jin, A. Bednarkiewicz, *Nanoscale* **2017**, *9*, 8288.
[12] E. C. Ximendes, W. Q. Santos, U. Rocha, U. K. Kagola, F. Sanz-Rodríguez, N. Fernández, A. D. S. Gouveia-Neto, D. Bravo, A. M. Domingo, B. Del Rosal, C. D. S. Brites, L. D.

Carlos, D. Jaque, C. Jacinto, *Nano Lett.* **2016**, *16*, 1695.
[13] R. Weissleder, *Nat. Biotechnol.* **2001**, *19*, 316.
[14] C.-H. Quek, K. W. Leong, *Nanomaterials* **2012**, *2*, 92.
[15] J. V. Frangioni, *Curr. Opin. Chem. Biol.* **2003**, *7*, 626.
[16] A. Benayas, B. Del Rosal, A. Pérez-Delgado, K. Santacruz-Gomez, D. Jaque, G. A. Hirata, F. Vetrone, *Adv. Opt. Mater.* **2015**, *3*, 687.
[17] F. J. A. Den Broeder, D. Kuiper, A. P. Van De Mosselaer, W. Hoving, *Phys. Rev. Lett.* **1988**, *60*, 2769.
[18] P. C. Fannin, S. W. Charles, *J. Phys. D. Appl. Phys.* **1989**, *22*, 187.
[19] M. Donolato, P. Antunes, R. S. Bejhed, T. Zardán Gómez De La Torre, F. W. Østerberg, M. Strömberg, M. Nilsson, M. Strømme, P. Svedlindh, M. F. Hansen, P. Vavassori, *Anal. Chem.* **2015**, *87*, 1622.
[20] K. Lodewijks, N. Maccaferri, T. Pakizeh, R. K. Dumas, I. Zubritskaya, J. Åkerman, P. Vavassori, A. Dmitriev, *Nano Lett.* **2014**, *14*, 7207.
[21] G. Armelles, A. Cebollada, A. García-Martín, J. M. García-Martín, M. U. González, J. B. González-Díaz, E. Ferreiro-Vila, J. F. Torrado, *J. Opt. A Pure Appl. Opt.* **2009**, *11*, 114023.
[22] B. Sepúlveda, J. B. González-Díaz, A. García-Martín, L. M. Lechuga, G. Armelles, *Phys. Rev. Lett.* **2010**, *104*, 147401.
[23] V. Bonanni, S. Bonetti, T. Pakizeh, Z. Pirzadeh, J. Chen, J. Nogués, P. Vavassori, R. Hillenbrand, J. Åkerman, A. Dmitriev, *Nano Lett.* **2011**, *11*, 5333.
[24] H. H. Jeong, A. G. Mark, T. C. Lee, M. Alarcon-Correa, S. Eslami, T. Qiu, J. G. Gibbs, P. Fischer, *Nano Lett.* **2016**, *16*, 4887.
[25] C. J. Behrend, J. N. Anker, B. H. McNaughton, R. Kopelman, *J. Magn. Magn. Mater.* **2005**, *293*, 663.
[26] J.-F. Berret, *Nat. Commun.* **2016**, *7*, 10134.
[27] K. Keshoju, H. Xing, L. Sun, *Appl. Phys. Lett.* **2007**, *91*, 123114.
[28] X. Wang, O. S. Wolfbeis, R. J. Meier, *Chem. Soc. Rev.* **2013**, *42*, 7834.
[29] G. Baffou, R. Quidant, *Laser Photonics Rev.* **2013**, *7*, 171.
[30] H. H. Richardson, M. T. Carlson, P. J. Tandler, P. Hernandez, A. O. Govorov, *Nano Lett.* **2009**, *9*, 1139.
[31] L. R. Hirsch, R. J. Stafford, J. A. Bankson, S. R. Sershen, B. Rivera, R. E. Price, J. D. Hazle, N. J. Halas, J. L. West, *Proc. Natl. Acad. Sci.* **2003**, *100*, 13549.
[32] A. M. Gobin, M. H. Lee, N. J. Halas, W. D. James, R. A. Drezek, J. L. West, *Nano Lett.* **2007**, *7*, 1929.
[33] S. Lal, S. E. Clare, N. J. Halas, *Acc. Chem. Res.* **2008**, *41*, 1842.
[34] V. Garcés-Chávez, R. Quidant, P. J. Reece, G. Badenes, L. Torner, K. Dholakia, *Phys. Rev. B - Condens. Matter Mater. Phys.* **2006**, *73*, 85417.
[35] X. Miao, B. K. Wilson, L. Y. Lin, *Appl. Phys. Lett.* **2008**, *92*, 124108.
[36] J. S. Donner, G. Baffou, D. McCloskey, R. Quidant, *ACS Nano* **2011**, *5*, 5457.

Supporting Information

SIMULTANEOUS LOCAL NANO-HEATING/THERMOMETRY BASED ON PLASMONIC MAGNETOCHROMIC NANODOMES

Zhi Li, Alberto Lopez-Ortega, Antonio Aranda-Ramos, José Luis Tajada, Jordi Sort, Carme Nogues, Paolo Vavasori, Josep Nogues, and Borja Sepulveda**

Figure S1. Schematic drawing of the fabrication steps of the nano-heater-thermometers (NHTs).

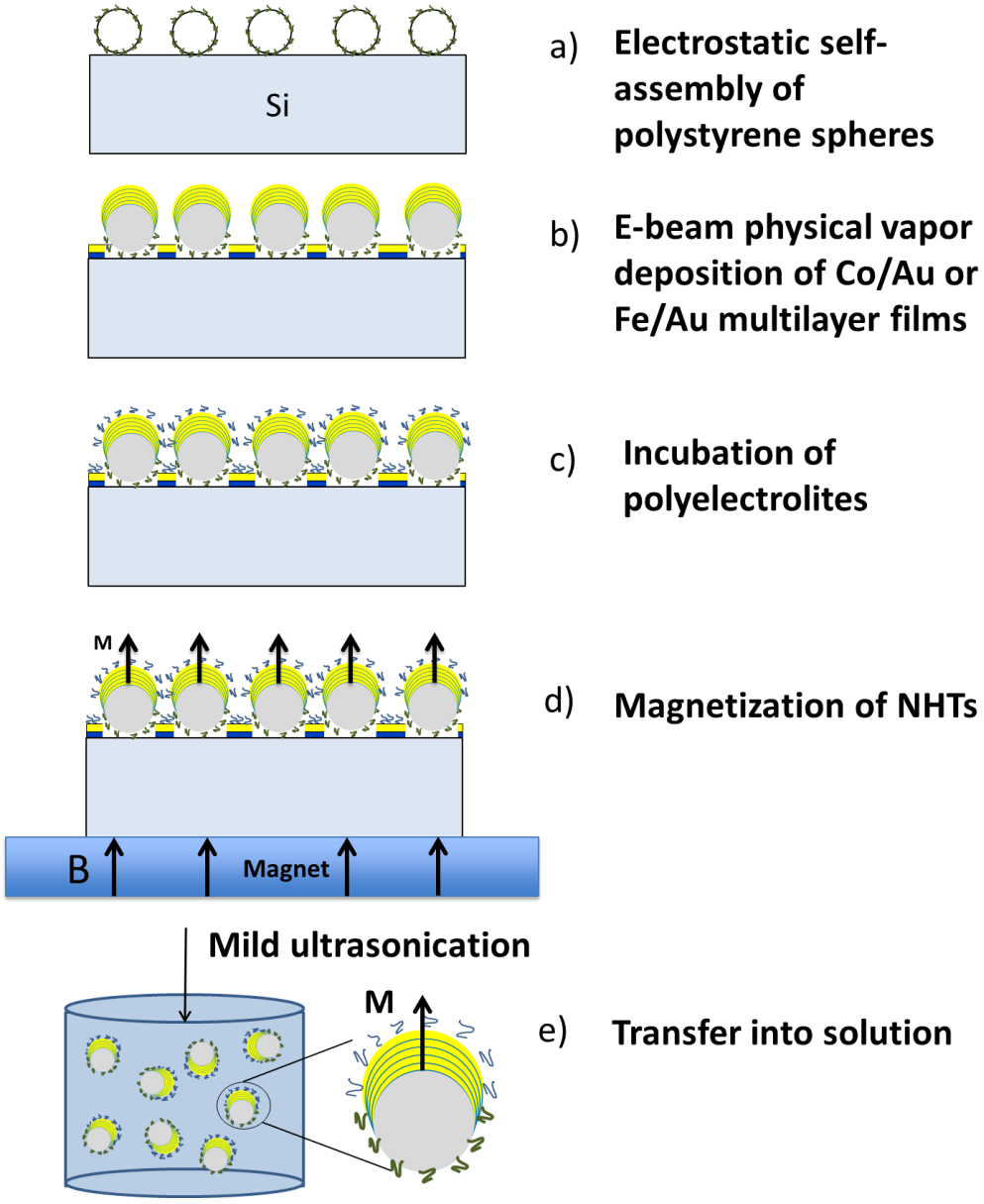

Figure S2. Room temperature out-of-plane hysteresis loop for the Co/Au nanodomes.

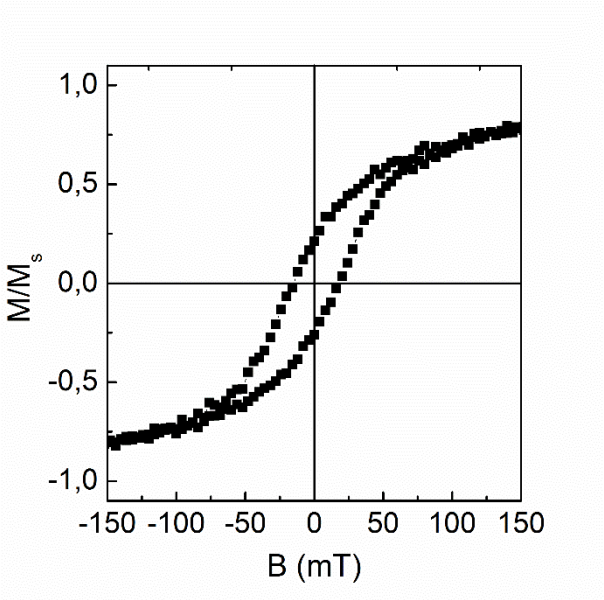

Figure S3. FDTD (Finite-difference time-domain) calculations of the extinction cross section C_{ext} of the Co/Au nanodomes in the perpendicular and parallel configurations of Figure. 1d.

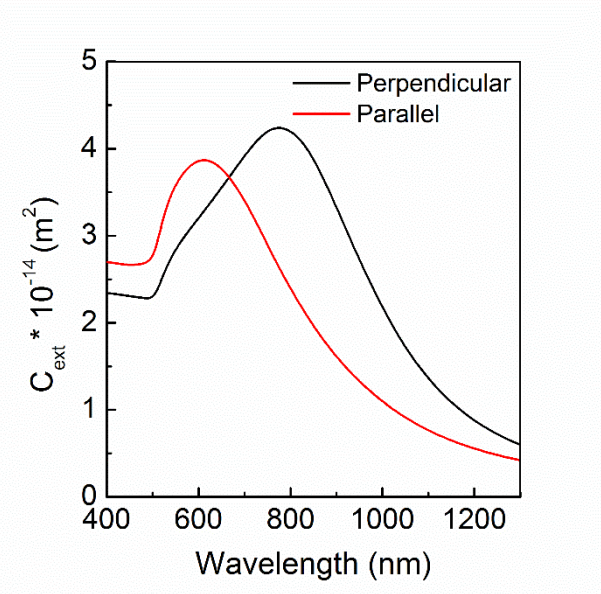

Figure S4. Differences in optical transmittance, Δτ, of the Co/Au nanodomes for different combinations of magnetic induction *B* direction and light polarization TM and TE. The particle concentration of colloidal dispersion is $1 \cdot 10^9$ nanodomes/mL.

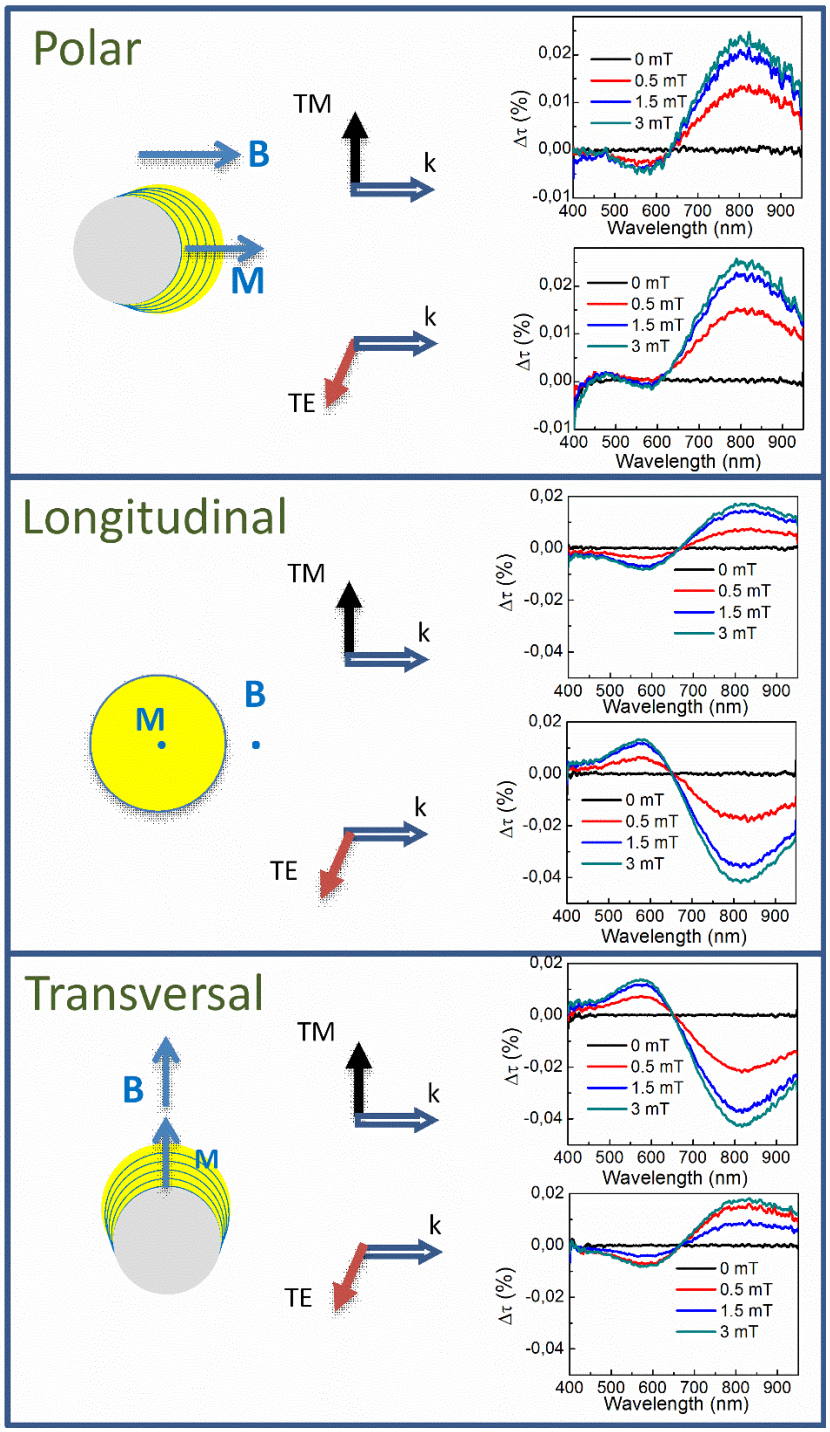

Figure S5. Amplitude (*A2n*ω) and phase (ϕ*2n*ω) of the mangetochromic signal, for different harmonics up to n = 3, as a function of the frequency of the ac magnetic induction with an rms amplitude of B = 2 mT. The particle concentration of colloidal dispersion is $1.5 \cdot 10^{10}$ nanodomes/mL.

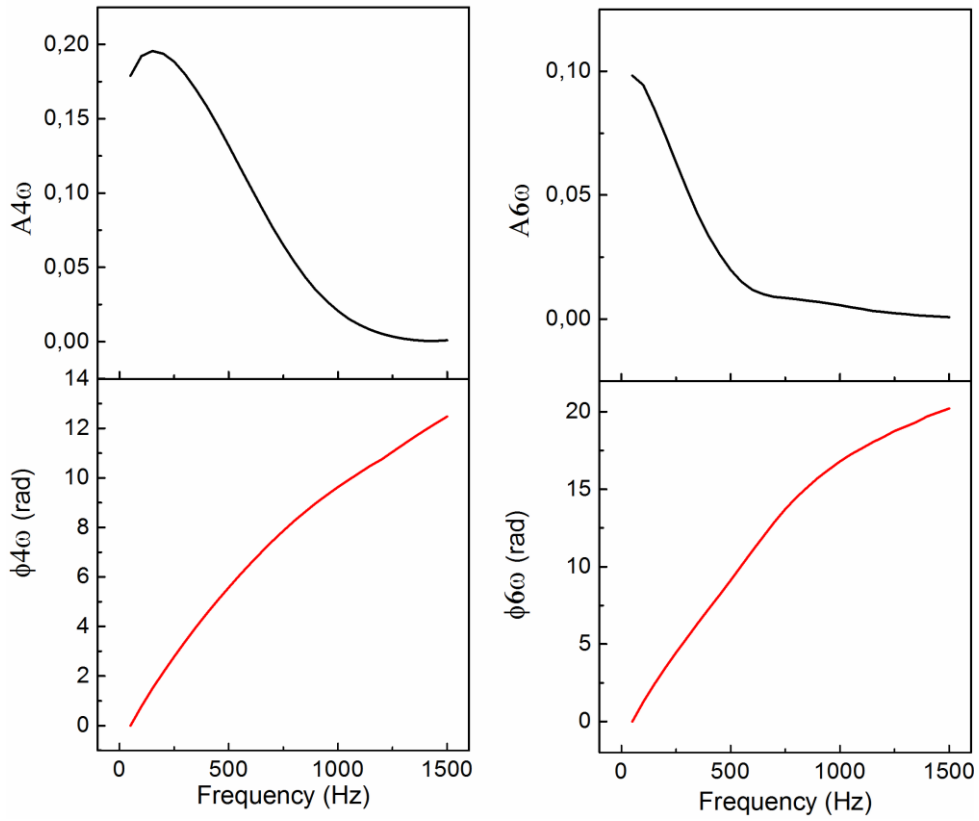

Figure S6. (a) UV-vis spectrum and (b) amplitude (*A2*ω) of second harmonic of the magnetochromic signal under an alternating magnetic induction (2 mT) for different concentrations of nanodomes.

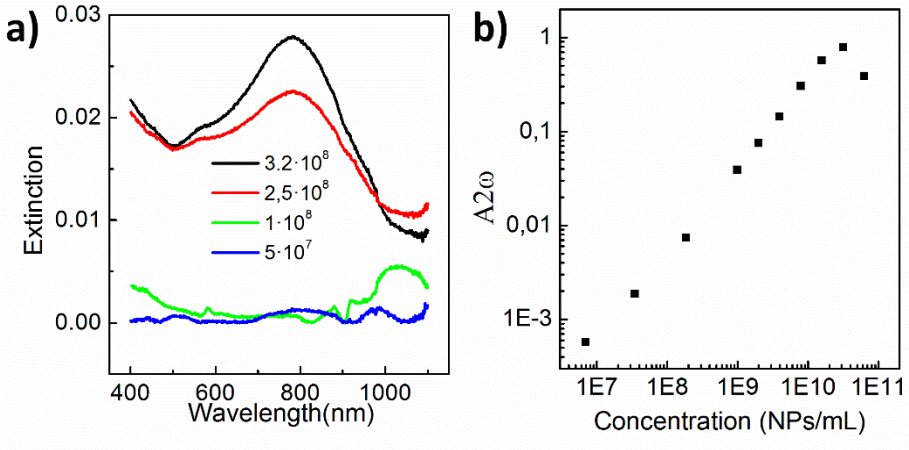

Figure S7. (a) Frequency dependence of *A*2ω for different liquid viscosities. Note the shift of the *A*2ω maxima to lower frequencies as the viscosity increases. (b) Determination of the sensitivity to changes of liquid viscosity, calculated as the phase lag change ($\Delta\phi 2\omega$) per viscosity variation ($\Delta\eta$) (from 1 to 2 mPa·s) as a function of the magnetic induction frequency. (B= 2 mT).

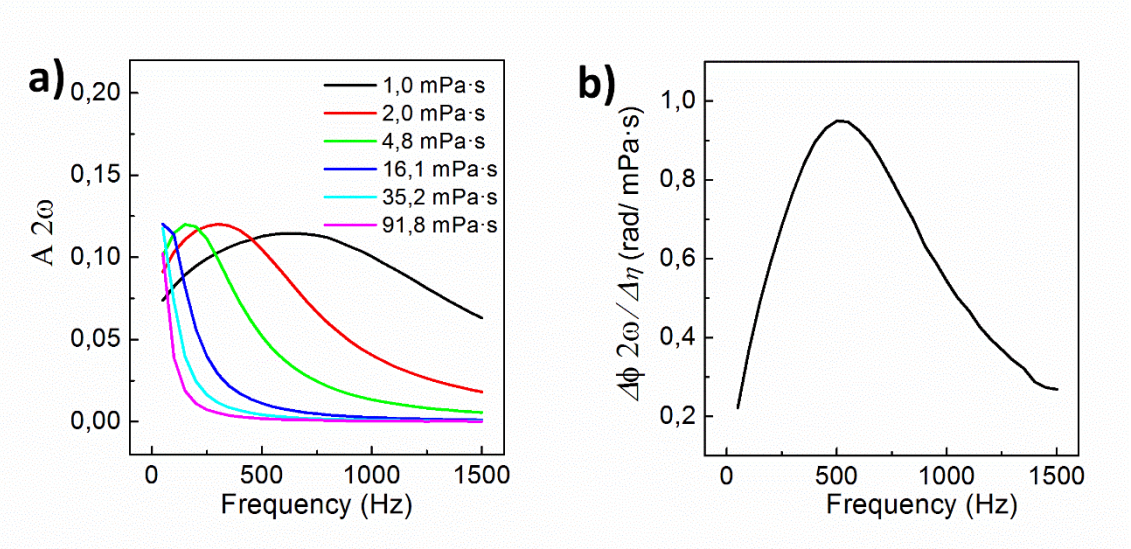

Figure S8. Analysis of the noise of the experimental setup during a real-time test of the phase ($\phi 2\omega$) under an ac magnetic induction (700Hz, 2mT). The standard deviation of the data is $5.3 \cdot 10^{-4}$ rad.

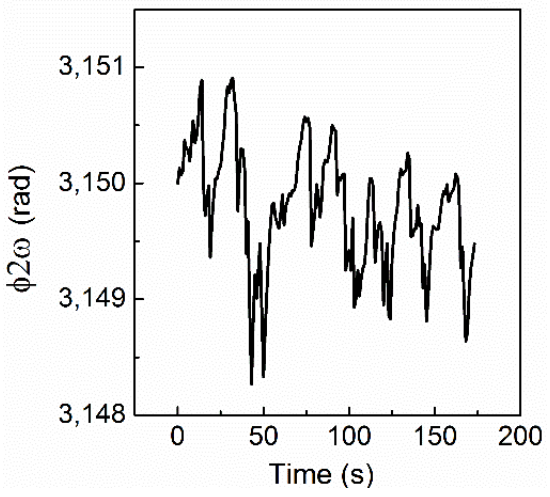

Figure S9. Sensitivity in the detection of temperature changes: variation of the phase lag ($\Delta\phi 2\omega$) induced by a temperature change (ΔT) as a function of the frequency (at B = 2mT) during Peltier heating (a), and optical heating (b) of the nanodomes.

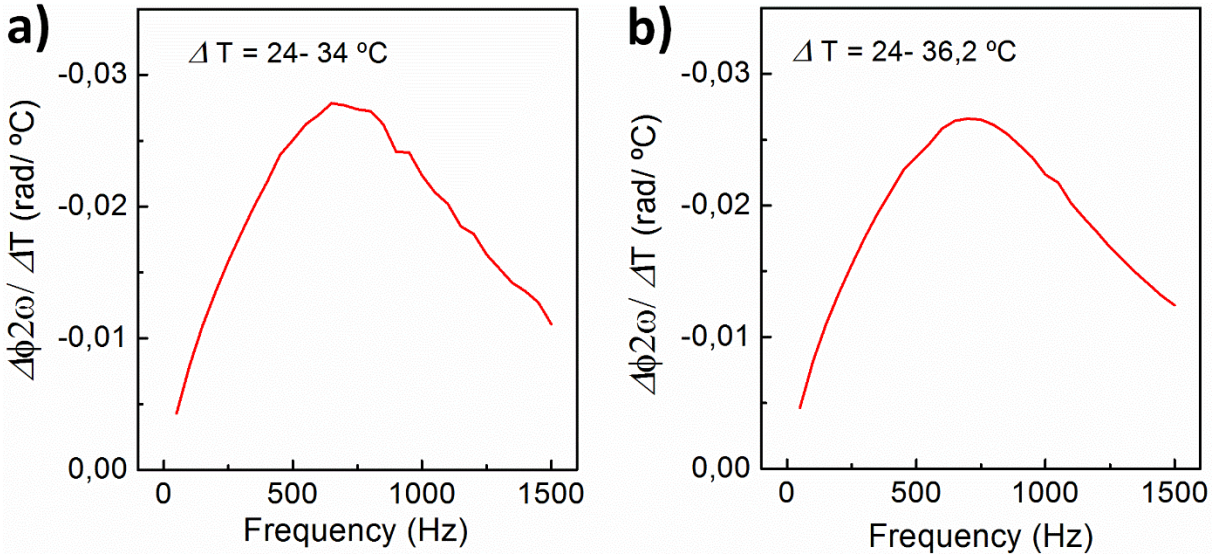

Figure S10. Comparative of the derivatives of the temperature with respect time (dT/dt) in the IR thermometer (IR Th) and nanodomes (ND) measurements when abrupt changes in the laser power from 25 mW to 315 mW and back to 25 mW are introduced, for either a collimated laser (left) or a focused laser (right).

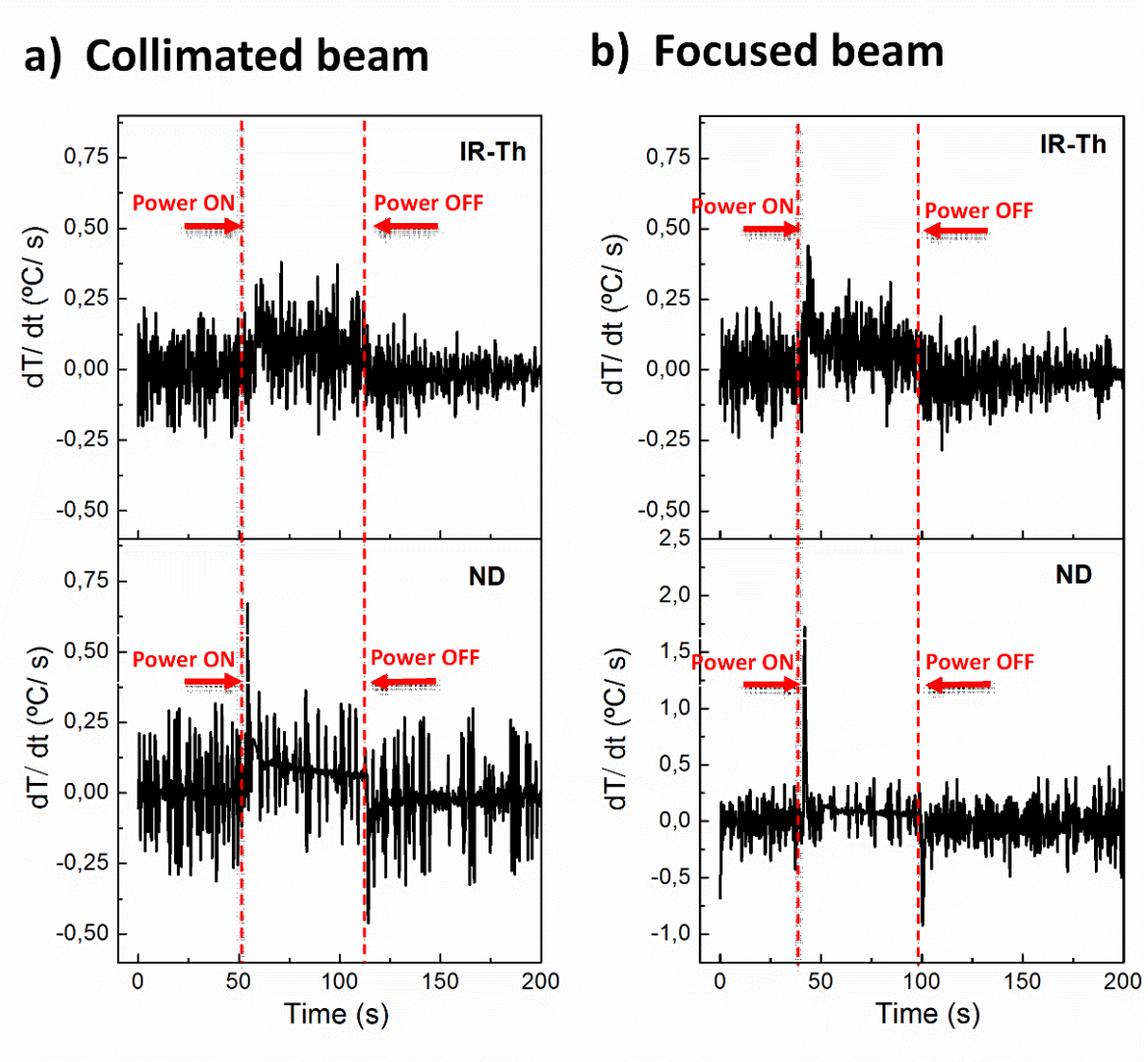

Figure S11. Long term stability test of the Co/Au nanodomes dispersed in cell medium (concentration $1.7 \cdot 10^9$ nanodomes/mL). Time dependence of the temperature (T) measured by the IR thermometer, and the phase ($\phi 2\omega$) and amplitude ($A2\omega$) of magnetochromic signal under an alternating magnetic induction (ω = 300 Hz, B = 2 mT).

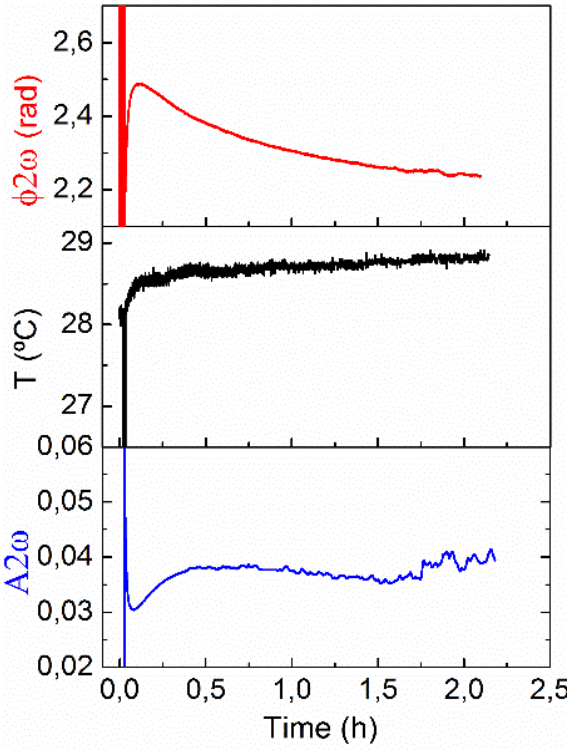

Figure S12. Demonstration of the simultaneous nano-heating/thermometry by Fe(5nm)/Au(35nm) nanodomes. a) Intensity modulation of the FeAu nanodomes at increasing magnetic induction frequencies (B = 2mT). b) Comparative of the amplitude (A2ω) and phase (ϕ2ω) for Co/Au and Fe/Au nandomes, showing the lower magneto-chromic effect in the latter due to their in-plane magnetization. c) Demonstration of the real-time detection of temperature variations induced by the 808 nm laser beam (noise 0.026ºC, i.e. detection limit of 0.08ºC) by the Fe/Au nanodomes.